Pergamon

0956-7151(94)00384-X

Acta metall. mater. Vol. 43, No. 4, pp. 1609–1617, 1995
Copyright © 1995 Elsevier Science Ltd
Printed in Great Britain. All rights reserved
0956-7151/95 $9.50 + 0.00

FATIGUE IN CERAMICS WITH INTERCONNECTING WEAK INTERFACES: A STUDY USING CYCLIC HERTZIAN CONTACTS

NITIN P. PADTURE† and BRIAN R. LAWN

Materials Science and Engineering Laboratory, National Institute of Standards and Technology, Gaithersburg, MD 20899, U.S.A.

(Received 10 June 1994)

Abstract—The deformation and fatigue of ceramics containing a contiguous network of weak interfaces is described. Observations of damage evolution within subsurface Hertzian compression fields in silicon carbide, alumina, and a glass–ceramic with dense, weakly bound platelet structures provide an experimental basis for the description. In a contact load–unload cycle, shear faults at the platelet interfaces undergo forward and reverse sliding. In cyclic loading, individual faults show evidence of frictional degradation, and the macroscopic damage zone undergoes progressive expansion. A sliding shear fault model with load–unload–reload hysteresis is developed to explain the results. Central to the model is the incorporation of resistive sliding tractions at the sliding interfaces, with allowance for progressive frictional attrition. A case study using fatigue data from the silicon carbide serves to illustrate the viability of the model.

1. INTRODUCTION

Polycrystalline ceramics can be toughened in the *long-crack* region by grain bridging [1–4]. Underlying this kind of toughening is microstructural heterogeneity, principally weak grain or interphase boundaries, to promote bridge formation, plus large grains and internal stresses, to reinforce pullout stresses [5]. The most effective bridging involves frictional sliding of contacting grain facets across the separating crack interface [2, 5–7]. However, these same microstructural heterogeneities tend also to diminish the *short-crack* toughness [8, 9], by providing easy fracture paths along weak interfaces under high local tensile stress. The short-crack region is critical to important mechanical properties like strength and flaw tolerance, wear and machinability.

A special class of grain-bridged ceramics is that in which weak interfaces so densely permeate the microstructure as to form a contiguous network. Of particular interest here are those macroscopically isotropic ceramics with densely packed platelets or needles bonded by a small amount of second phase. Microstructural failure occurs by shear-induced decohesion and sliding along "closed" (i.e. mutually contacting) boundary facets. At applied stress concentrations, linkage and coalescence between neighboring failure facets occur readily, leading ultimately to material removal. This phenomenon of interconnecting microfracture is the basis of so-called "machinable ceramics" [10–14]. Such materials, insofar as their fracture tendency is dominated by damage accumulation rather than extension of a single well-developed crack, tend to be nonlinear in their stress–strain response and dissipative in their energy absorption.

The question arises as to the fatigue properties of such ceramics. With ordinary bridging ceramics the concern is that the contacts between sliding grains may be especially susceptible to reduced shielding by degradation in cyclic loading, and thence to loss of toughness. Definitive evidence for intergrain degradation, in the form of frictional debris, has been observed in *in situ* experiments in the scanning electron microscope at bridging sites in alumina using conventional long-crack cyclic specimens [6]. Similar frictional debris has been observed in the notch regions of compact tension specimens loaded in cyclic compression [15, 16]. However, the relevance of long-crack fatigue test configurations to short-crack properties remains to be demonstrated. Are the individual microfractures in a ceramic with interconnecting weak interfaces subject to the same kind of frictional degradation process?

Recent contact damage studies on a range of ceramics [17–22] provide some insights into the issue of short-crack fatigue. These studies employ a simple Hertzian test, wherein an indenting sphere is subjected to repeat loading on a flat ceramic specimen surface. Cumulative damage events at the microscale are readily observable. In relation to the ceramic microstructure the key finding of the Hertzian studies

†Guest Scientist, from Department of Materials Science and Engineering, Lehigh University, Bethlehem, PA 18015, U.S.A. Now with University of Connecticut, Storrs, CT 06269, U.S.A.

may be summarized thus: as the long-crack toughness increases by introduction of weak boundaries, so does the fundamental nature of the indentation damage change, from tensile-driven macroscopic cone cracks outside the contact area to distributed shear microdeformation and microfracture in the subsurface compression zone [17, 23]. Again, the existence of weak boundaries is central to the development of the latter kind of damage zone, providing favorable sites for local intergranular shear failures in the subsurface contact field. The damage accumulates with repeat loading, leading to strength degradation [18, 24] and in extreme cases to material removal [24, 25].

In the present paper we document Hertzian contact fatigue in ceramics containing an interconnecting network of weak boundaries. Observations of cumulative subsurface damage in a silicon carbide composite with *in situ* grown elongate grains and weak interphase boundaries are presented as a case study. Some additional observations on other materials, i.e. an alumina–calcium hexaluminate composite and a machinable glass–ceramic, are included to demonstrate generality. A closed shear fault model for describing the response of individual damage elements within the Hertzian field is proposed. The fault model centers around a sliding intergranular interface with frictional shear tractions. These tractions are assumed to degrade with number of contact cycles, resulting in enhanced decohesion and thence coalescence with neighboring fault interfaces, with consequent fatigue of the structure.

2. BACKGROUND EXPERIMENTAL OBSERVATIONS OF SUBSURFACE HERTZIAN CONTACT DAMAGE

In this section we present pertinent observations of contact fatigue damage in selected bridging ceramics containing a high density of weak interfaces, specifically using the Hertzian indentation test. We aim specifically to identify the controlling nonlinear–dissipative elements of deformation and fatigue in the microstructures.

2.1. Materials

Three *in situ* toughened materials are chosen for study, with a special focus on the first. These materials have in common a contiguous platelet structure, macroscopically isotropic in orientation, with weak interfaces between the platelets and included second phases.

2.1.1. Silicon carbide composite. This is a designed microstructure consisting of ~80 vol.% elongate SiC grains ~3 μm thick by ~25 μm long, with ~20 vol.% yttrium aluminum garnet (YAG) grain boundary phase [22, 26]. High thermal expansion mismatch stresses ~1 GPa and weak interphase boundaries ensure intergranular fracture in this material [26].

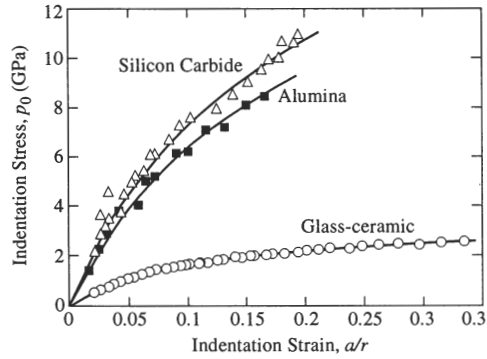

Fig. 1. Indentation stress–strain curves for *in situ* processed silicon carbide composite, alumina–calcium hexaluminate composite, and mica–containing glass–ceramic. Data obtained using tungsten carbide spheres of radius $r = 1.98$–12.70 mm. Solid curves are empirical fits through the data. Note significant deviation from linear Hertzian elastic response. (Alumina data courtesy of L. An and H. M. Chan, silicon carbide and glass–ceramic data from Ref. [23].)

2.1.2. Alumina–calcium hexaluminate composite. This is a designed ceramic microstructure, with ~70 vol.% equiaxed Al_2O_3 grains ~20 μm diameter and ~30 vol.% $CaO \cdot 6Al_2O_3$ embedded platelets ~30 μm long and ~4 μm thick (courtesy L. An and H. M. Chan).

2.1.3. Mica-containing glass–ceramic. This is a commercial machinable glass–ceramic (Macor, Corning Inc., Corning, N.Y.) [10–12], with ~55 vol.% interlocking fluorophlogopite mica flakes 10 μm long and 1–2 μm thick in a matrix of ~45 vol.% borosilicate glass. The mica flakes with their weak basal cleavage and matrix interfaces facilitate easy microfracture.

2.2. Indentation stress–strain curves

The Hertzian test can be used in single-cycle loading to obtain "indentation stress–strain curves" for any given material [17, 27]. In this test a tungsten carbide sphere is used to produce contact damage in a flat specimen surface. At prescribed values of load P and sphere radius r, contact radii a are measured from impressions left in thin metal coatings on polished specimen surfaces [17]. These measurements enable plots of mean indentation

Fig. 2. On facing page. Optical micrographs in Nomarski illumination showing half-surface (top) and section (bottom) views of Hertzian contact sites in silicon carbide composite: number of cycles (A) $n = 1$; (B) $n = 10^1$; (C) $n = 10^2$; (D) $n = 10^3$; (E) $n = 10^4$; (F) $n = 10^5$; (G) $n = 10^6$. Peak contact stress $p_0^* = 6.0$ GPa, using WC sphere of radius $r = 3.18$ mm at load $P = 1000$ N and frequency 10 Hz. Note appearance of radial crack (arrow) from surface contact zone in (G). (After Ref. [24].)

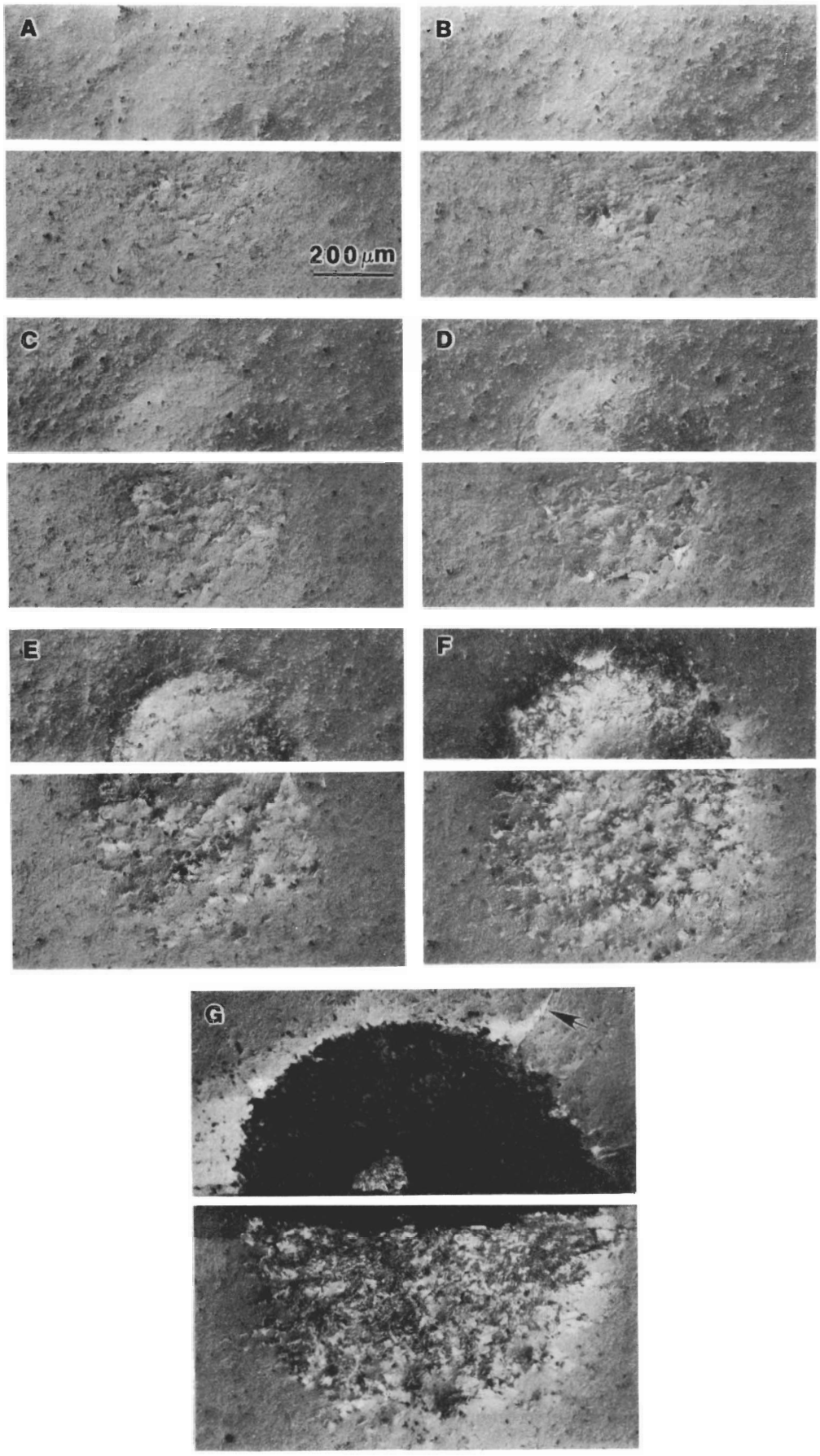
A
B
200 μm
C
D
E
F
G

pressure $p_0 = P/\pi a^2$ vs indentation strain a/r to be constructed. Deviations from the linear response predicted by the classical Hertzian elasticity equations [17, 27] then provide a measure of the material "ductility" [23].

Plots of indentation stress–strain curves for the three test materials are shown in Fig. 1. Significant nonlinearities are indeed observed in all three cases, indicating the activity of dissipative deformation processes [27, 28].

2.3. Observations of contact damage

A principal advantage of the Hertzian test is its capacity to reveal the fundamental deformation–fracture properties in a highly controlled manner [4]. The ensuing damage patterns are readily observable at completion of contact by conventional microscopic techniques, and their evolution during contact monitored by acoustic emission. Most important, the test is readily amenable to repeat loading, enabling the study of cyclic fatigue damage [17].

Figure 2(A)–(G) illustrates fatigue damage patterns in the silicon carbide composite, for $n = 1$ to 10^6 cycles at a peak contact stress $p_0^* = 6.0$ GPa [24]. In this sequence the half-surface (upper) and section (lower) views are obtained using "bonded-interface" specimens [18, 19], prepared as follows: (i) two polished rectangular half-blocks are glued together at their side faces with thin adhesive; (ii) indentations are made on the polished top surface symmetrically across the trace of the bonded interface; (iii) the adhesive is dissolved in solvent and the half-blocks separated; (iv) the contact regions are viewed in Nomarski illumination. The density and size of the damage zone show a dramatic increase with number of cycles, from modest damage at $n = 1$ to near-crater formation, with attendant radial cracks, at $n = 10^6$. Also notable in the section views is the onset of damage at some distance *below* the contact area, coresponding to the region of maximum shear stress [17]. In these tests, acoustic activity during the first loading half-cycle begins above $p_0 \sim 3$ GPa and increases strongly up to the peak $p_0^* = 6.0$ GPa, indicating a proliferation of microdeformation events beyond some incubation pressure; lesser, but not insignificant, activity also occurs below $p_0 \sim 2$ GPa during the first and each subsequent unloading half-cycle, indicating some reversal in the deformation process [24].

Figure 3 shows higher magnification views of the damage in the silicon carbide after $n = 10^6$ cycles, from the near-center region of the subsurface zone in the section of Fig. 2(G). There is clear evidence of failure at some of the SiC–YAG interfaces. Material has been dislodged from the surface, and copious subgrain-scale debris is visible. The indications of interfacial frictional degradation by forward–reverse sliding is compelling. In this context, recall from Section 1 the previously reported observations of

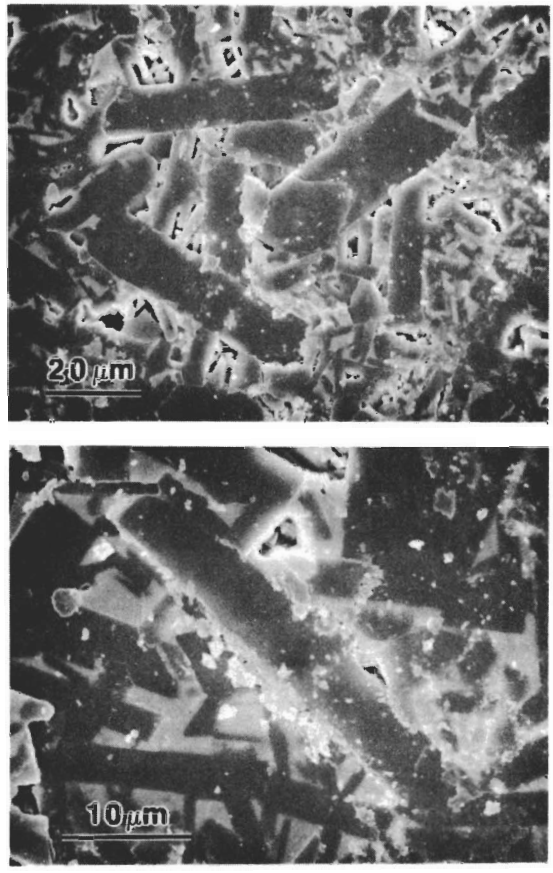

Fig. 3. Scanning electron micrographs of Hertzian contact damage in silicon carbide composite after 10^6 cycles, taken from center regions of subsurface damage zones in Fig. 2(G). Note surface cavities from material removal and sliding-interface debris.

frictional debris at bridging grains in long-crack specimens of alumina [6, 15, 16].

Comparative micrographs for the alumina composite, Fig. 4, and the glass–ceramic, Fig. 5, after $n = 10^5$ cycles reveal analogous sliding-interface damage mechanisms.

3. MODEL OF FATIGUE BY FRICTIONAL DEGRADATION OF WEAK INTERFACES IN HERTZIAN CONTACT FIELD

In this section we construct a phenomenological model for fatigue damage in ceramics with a high density of weak interfaces, with specific reference to Hertzian contact fields. Previous models of Hertzian-induced damage in bridging ceramics [29] center around a generic two-step deformation–fracture element embedded in the subcontact compression zone, i.e. a closed shear fault with extensile cracks at its ends [30–33]. Such two-step models are valid for those material types where individual faults are well separated from their neighbors, so that secondary crack link-up is a necessary component of macrocrack formation ("dilute" fault density). In the platelet materials of interest here neighboring shear faults

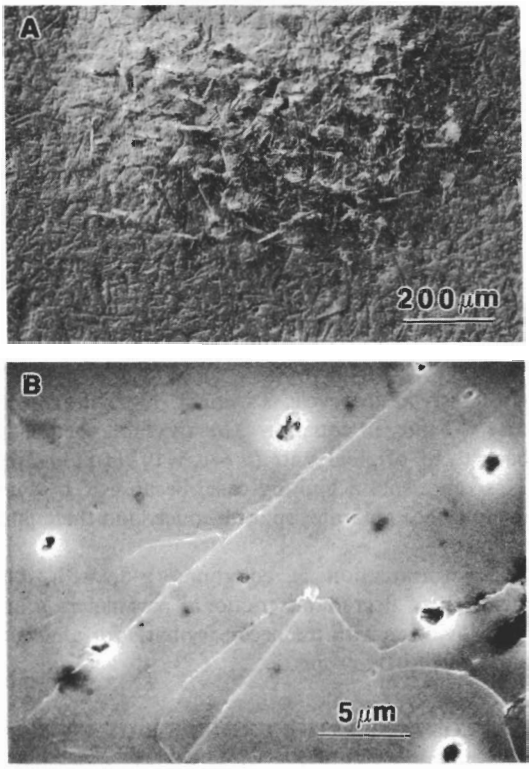

Fig. 4. (A) Optical and (B) scanning electron microscope views of contact damage in alumina–calcium hexaluminate composite $n = 10^5$ cycles. Peak contact stress $p_0^* = 5.6$ GPa, using WC sphere of radius $r = 3.18$ mm at load $P = 1000$ N and frequency 10 Hz. (Courtesy of L. An and H. M. Chan.)

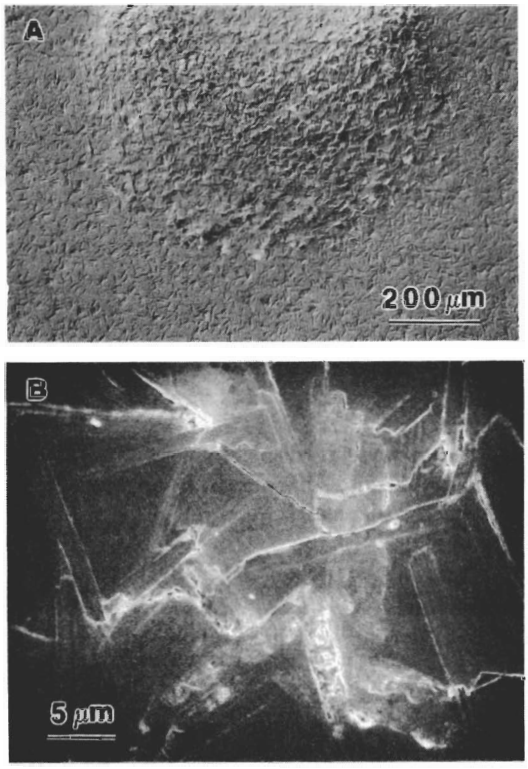

Fig. 5. (A) Optical and (B) scanning electron microscope views of contact damage in mica-containing glass ceramic after $n = 10^5$ cycles. Peak contact stress $p_0^* = 1.63$ GPa, using WC sphere of radius $r = 3.18$ mm at load $P = 500$ N and frequency 10 Hz. (Courtesy of H. Cai.)

effectively overlap one another, so extensile cracking is no longer essential. Accordingly, our analysis takes as its central element a simple closed shear fault located at an interphase boundary, with frictional tractions at the interface, Fig. 6. Some characteristic microstructural dimension l, e.g. platelet length, determines the scale of the fault. Reverse sliding may be activated during unloading if the peak contact pressure is sufficiently high, allowing for hysteresis in the loading–unloading–reloading cycle.

3.1. *Stress field*

The closed-fault system of Fig. 6 slides under the driving action of resolved shear stresses in the subsurface Hertzian field. These shear stresses are determined as a differential in principal normal stresses σ_1 and σ_3, with $\sigma_3 < \sigma_1$ everywhere and σ_1 and σ_3 both compressive (negative) in the subsurface contact zone [34]. Let us define dimensionless α coefficients, positive in this compression zone, by normalizing the stresses to the mean Hertzian contact pressure $p_0 = P/\pi a^2$

$$-\sigma_1 = \alpha_1 p_0 \tag{1a}$$

$$-\sigma_3 = \alpha_3 p_0. \tag{1b}$$

Sliding in any direction is opposed by frictional stresses, augmented by any internal residual stresses σ_R, at the interface. Following the lead of rock and soil mechanics [35], the *net* resolved shear stresses on the forward (+) and backward (−) sliding fault in Fig. 6 may be written [29]

$$\sigma_F^+ = [\tfrac{1}{2}(\alpha_3 - \alpha_1)\sin 2\Psi]p_0 - \mu\{[\tfrac{1}{2}(\alpha_3 + \alpha_1) - \tfrac{1}{2}(\alpha_3 - \alpha_1)\cos 2\Psi]p_0 - \sigma_R\} - \tau_c \tag{2a}$$

$$\sigma_F^- = [\tfrac{1}{2}(\alpha_3 - \alpha_1)\sin 2\Psi]p_0 + \mu\{[\tfrac{1}{2}(\alpha_3 + \alpha_1) - \tfrac{1}{2}(\alpha_3 - \alpha_1)\cos 2\Psi]p_0 - \sigma_R\} + \tau_c \tag{2b}$$

where Ψ is the angle between the fault plane and the σ_3 axis, μ is a coefficient of friction, τ_c is a critical "cohesion" or "adhesion" stress. The first composite

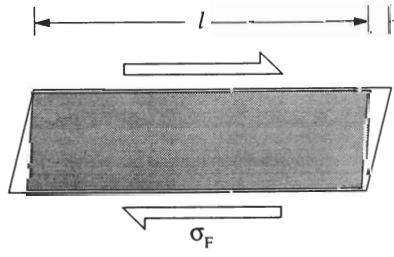

Fig. 6. Closed shear fault at sliding intergrain boundary of length l, at shear stress σ_F and displacement u. Shear stress at interface drives sliding, compression stress maintains closure.

term on the right side of equation 2 is the shear stress from the Hertzian field resolved on the fault plane. The remaining composite terms are from a Coulomb resistance law [35, 36]: term two is a friction contribution from the corresponding resolved compressive normal stress plus residual stress; term three is the adhesion stress, i.e. the minimum shear stress needed to cause sliding. Note that since $\alpha_3 > \alpha_1$ always, the square bracket terms in equation 2 are positive always in the compression zone.

3.2. Sliding shear fault

We now derive constitutive relations for forward and backward sliding. The shear fault stress σ_F in equation 2 increases as p_0 increases, providing an internal wedging displacement u for the crack extension. This displacement is opposed by the confining elastic matrix, according to a Hookean relation [29]

$$\sigma_F = \kappa u \tag{3}$$

with κ an elastic stiffness term. Equations 2 and 3 lead to linear functions $p_0(u)$ for our forward (+) and backward (−) slipping fault:

$$p_0^+ = 2(\kappa u + \tau_C - \mu\sigma_R)/\{[(\alpha_3 - \alpha_1)\sin 2\Psi - \mu[(\alpha_3 + \alpha_1) - (\alpha_3 - \alpha_1)\cos 2\Psi]\} \tag{4a}$$

$$p_0^- = 2(\kappa u - \tau_C + \mu\sigma_R)/\{[(\alpha_3 - \alpha_1)\sin 2\Psi + \mu[(\alpha_3 + \alpha_1) - (\alpha_3 - \alpha_1)\cos 2\Psi]\}. \tag{4b}$$

These functions are plotted in Fig. 7 as the inclined upper (+) and lower (−) light lines for an initial loading–unloading–reloading cycle. (We show Fig. 7 with calibrated axes, but defer discussion of the calibration procedure to the next section and consider only qualitative features here.) The path traversed by the fault in $p_0(u)$ space is indicated by the heavy lines with arrows: inclined segments denote fault sliding branches; vertical segments denote stationary branches. In the case shown, the peak load p_0^* is sufficiently high that reverse sliding occurs during unloading, i.e. $u^* > u_0$: u^* corresponds to the peak displacement along the upper (+) line, and is obtained at $p_0^+ = p_0^*$ in equations 2(a) and 3; u_0 corresponds to the remnant displacement at full unloading along the lower (−) line, and is obtained at $p_0^- = 0$ in equations 2(b) and 3

$$\kappa u^* = \tfrac{1}{2}\{(\alpha_3 - \alpha_1)\sin 2\Psi - \mu[(\alpha_3 + \alpha_1) - (\alpha_3 - \alpha_1)\cos 2\Psi]\}p_0^* - (\tau_C - \mu\sigma_R) \tag{5a}$$

$$\kappa u_0 = \tau_C - \mu\sigma_R. \tag{5b}$$

Hysteresis in the cycle is evident. Note the special case $\tau_C = \mu\sigma_R$ in equation 5(b): the fault then slides back to its original state ($u = u_0 = 0$) on unloading. This represents a limiting case, because if $\tau_C < \mu\sigma_R$ the interface separates spontaneously and there is no contact.

The formulation in equations 1–5, with their inclusion of degradable frictional parameters μ and τ_C, provide us with the necessary basis for an evaluation of fatigue properties.

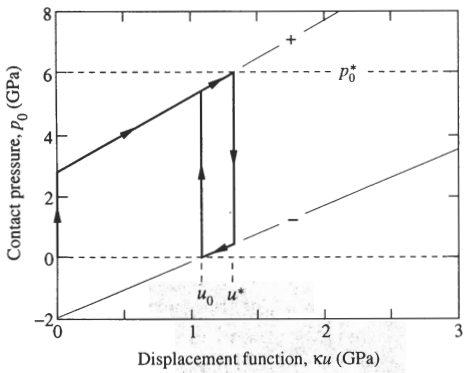

Fig. 7. Constitutive relation for shear fault displacement u as function of Hertzian contact pressure p_0, for single load–unload–reload cycle in silicon carbide composite. Inclined light lines represent equilibrium relations for forward (+) and reverse (−) sliding. Solid segments represent cyclic path, showing unload–reload hysteresis between displacements u_0 and u^*.

4. CONTACT FATIGUE CASE STUDY ON SiC

In this section we illustrate the capacity of the model to account for the contact fatigue, with special reference to the SiC composite material described in Section 2. We start with a parametric "calibration" of equations 1–5 from single-cycle data, and go on to use this calibration as a basis for evaluating the ensuing cycle degradation.

Some of the parameters are predetermined. The α coefficients follow directly from knowledge of the Hertzian stress field [37]. We compute these coefficients at the point of maximum shear stress, about $0.5a$ directly below the contact center. There is a slight dependence on Poisson's ratio: taking $\nu = 0.19$ for SiC, we obtain $-\sigma_1/p_0 = \alpha_1 = 0.23$ and $-\sigma_3/p_0 = \alpha_3 = 1.20$ in equation 1 [37]. At this same point along the contact axis (coincident with the σ_3 trajectory [34]) the fault orientation for maximum shear is $\Psi = 45°$. To evaluate the internal residual stress, we treat the structure as a contiguous SiC network with included YAG second phase: taking composite Young's modulus $E = 350$ GPa [22], differential expansion coefficient $\Delta\alpha = \alpha(\text{YAG}) - \alpha(\text{SiC}) = 5.1 \times 10^{-6}$ [26], and temperature differential $\Delta T = 1100°C$, we have $\sigma_R = \frac{1}{2}E\Delta\alpha\Delta T = +1.0$ GPa. Clearly, the values of these parameters will not remain constant for all fault locations and orientations through the damage zone—we have chosen the most favorable case for sliding in the interest of conservative prediction.

This leaves just two adjustable parameters, the friction terms μ and τ_C, to complete our determination of the constitutive relations in equation 4 and of the corresponding displacement limits in equation 5 for the silicon carbide composite. We set first-cycle

values $\mu(1) = 0.10$ and $\tau_C(1) = 1.2$ GPa to match as well as possible the onset of forward sliding at $p_0 > 3$ GPa during initial loading and reverse sliding at $p_0 < 2$ GPa during initial unloading, as indicated by the acoustic activity observations mentioned in Section 2.3 [24]. These are the parametric values actually used to plot Fig. 7, at a peak contact stress $p_0^* = 6.0$ GPa.

We can now describe how degradation may occur through progressive attrition of frictional tractions with number of cycles [6, 38]. A first-principles derivation of a suitable degradation relation requires fundamental information on the underlying processes. In the absence of such information we employ an empirical formulation for substitution into equations 4 and 5. The simplest such formulation corresponds to a linear attrition rate, as defined by $\mu(n) = \beta(n)\mu(1)$ and $\tau_C(n) = \beta(n)\tau_C(1)$, with a degradation coefficient

$$\beta = 1 - (n-1)/(N-1) \qquad (6)$$

where N is the number of cycles for total degradation.

Accordingly, in Fig. 8 we plot hysteretic unload–reload loops for several values of β for our silicon carbide composite. At the upper limiting value $\beta = 1$ ($n = 1$), the loop reproduces the zero degradation unload–reload configuration of Fig. 7. At the lower limiting value $\beta = 0$ ($n = N$), the loop condenses onto a straight line through the origin, corresponding to frictionless sliding, i.e. total degradation. As β diminishes (n increases) within these limits, i.e. as degradation proceeds, the hysteresis loop widens and flattens out. In this description, the widening differential between displacements u^* and u_0 (equation 5, cf. Fig. 7) provides a measure of microstructural "loosening" during cycling. These two displacements are plotted in Fig. 9 as a function of $\log n$, assuming $N = 2 \times 10^6$ for total degradation. Two sets of curves are shown, for the value $\sigma_R = 1$ GPa used above and for $\sigma_R = 0$. In this material, the enhancement of shear displacements by the residual tensile stresses is ultimately dwarfed by the influence of the frictional degradation. The trend to rapid degradation as n approaches N on the logarithmic scale of Fig. 9 is consistent with the rate of damage accumulation observed in the micrograph sequence of Fig. 2.

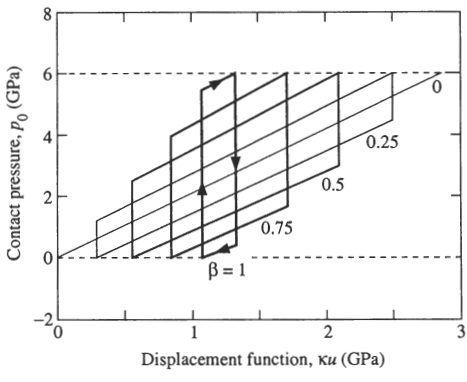

Fig. 8. Same as Fig. 7, but showing how unload–reload hysteresis loop widens and flattens as degradation coefficient β degrades with cycling.

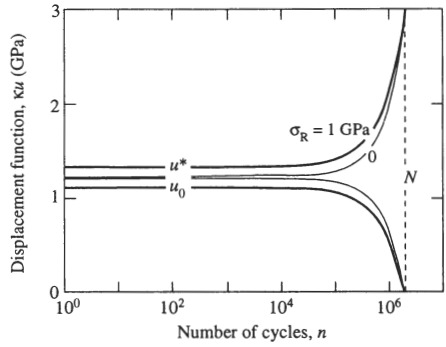

Fig. 9. Plot of displacements u_0 and u^* [equation 5(a) and 5(b)] as function of number of cycles for silicon carbide composite. Calculation assumes linear fall-off in friction (equation 6), to zero at $N = 2 \times 10^6$ (total degradation state). Computed for two internal residual stresses σ_R. Note rapid increase in displacements after $n \sim 10^5$ cycles [cf. Fig. 2(F)].

5. DISCUSSION

We have described the deformation and fatigue of ceramics containing a contiguous network of weak interfaces, with specific reference to Hertzian contacts on ceramics with densely packed platelet structures. At the core of the damage process is forward–reverse frictional sliding along microstructurally discrete weak interfaces in the subsurface compression–shear contact field (Fig. 6). Hysteresis in the unload–reload cycle, with progressive frictional attrition, accounts for the observed fatigue degradation.

The closed shear fault model described in Section 3 has a fundamental commonality with models developed for other kinds of heterogeneous brittle solids [29–33, 35]. In rocks and concrete and porous ceramics the shear faults preexist as part of the extrinsic defect structure [33, 35]. In high density ceramics, e.g. alumina and silicon nitride, the faults are stress-induced and material-intrinsic, e.g. preferred intragranular slip planes or twins [17, 21, 29]. All such faults, extrinsic or intrinsic, are governed by the kind of generic frictional tractions defined in equation 2. As indicated earlier (Sections 1 and 3), in most of these other solid types accompanying extensile cracks are an essential component of the modeling. In the present class of materials, extensile cracking is relatively unimportant because the shear faults overlap their neighbors, and macroscopic cracks can evolve simply by interconnection and subsequent opening of the faults themselves.

If our shear fault model is generic, it is also phenomenological. In writing equation 2 we have presumed an empirical Coulomb criterion for sliding friction, as used in rock and soil mechanics [35]. We have not considered the fundamental nature of

the friction process at all in this study. The importance of friction in cyclic contact fatigue is evident from the presence of surface debris, most notably in Fig. 3. This kind of persistently adhering debris product is symptomatic of severe wear at highly stressed sliding facets [6, 39]. The roles of interface roughness, surface chemistry, electrostatic interactions, and other variables in these wear processes hold remain to be determined.

Certain issues concerning the damage mechanics are not addressed by the present model. It is assumed in our analysis that the interfacial sliding in Fig. 6 occurs uniformly along the length of the facet. In reality, a shear crack must first initiate from some nucleation site and spread along this interface, in much the same way as fiber–matrix debonding occurs in reinforced composites. An attendant issue is the manner in which the shear strains caused by the interfacial sliding are accommodated by the structure. Some of this deformation could be relieved by block slip or twinning in the sheared grains. In the absence of any such relief mechanism, the strain must be accommodated by cracks or cavities, resulting in some dilatancy [35, 40]. There is some evidence of cavity formation at platelet interfaces in the present SEM views of Fig. 3, as well as in earlier subsurface studies of Vickers indentation damage in other materials (zinc sulphide) [41].

Another issue is that of stochastics. In our computations of Section 4 we chose parameters corresponding to most favourable conditions for sliding. In reality, these parameters must vary spatially within the subsurface zone, because of inherent inhomogeneity in the Hertzian field [34] and variability in interface orientation relative to the principal stress trajectories [29]. We should therefore expect individual sliding events to initiate sequentially rather than simultaneously during any load–unload cycle, so that the cumulative manifestation of a population of discrete elements with straight-segment hysteresis loops (Figs 7 and 8) is a smoothed-out indentation stress–strain curve (Fig. 1).

There is the further question as to why the damage zone expands in size as well as in density during cyclic fatigue sequences such as that in Fig. 3. As frictional degradation occurs at the sliding fault interfaces within the initial damage zone so does the rigidity of the damage zone diminish, transferring more of the contact load to the surrounding material. The faults in this adjacent region are themselves now susceptible to sliding, so the damage zone spreads. In fixed-load cycling, the contact area itself expands as the material continues to "soften", reinforcing the effect.

There are some implications from the analysis concerning the tailoring of densely packed, contiguous platelet or needle microstructures for specific material applications. The most crucial element is the interfacial toughness of the platelet (needle) boundaries. If sufficiently weak, these boundaries fail readily in local compression–shear fields, with enhanced capacity for absorbing impact energy by damage accumulation. The material is also rendered potentially machinable [42]. Conversely, the material becomes susceptible to fatigue and wear [24] (Fig. 3). The nature of the bonding between the platelets (needles) and any second phase in the microstructure becomes a critical issue. Internal tensile mismatch stresses may enhance fatigue degradation by opening up the sliding interfaces, although the effect will be insignificant if $\mu\sigma_R \ll \tau_C$ in equations 4 and 5 (cf. $\mu\sigma_R = 0.1$ GPa, $\tau_C = 1.2$ GPa, for our silicon carbide ceramic in Section 4). Note that grain size does not enter into the model of Section 3, so there is an implied absence of any microstructural scaling effect in the sliding micromechanics. The same is certainly not true of materials in which the growth of extensile cracks from the shear faults is an important component of the damage process, where grain size is acknowledged as a critical factor in the crack initiation [29].

Acknowledgements—Data in Figs 1 and 4 on the alumina–calcium hexaluminate were kindly provided by L. An and H. M. Chan, and in Figs 1 and 5 on the mica-containing glass–ceramic by H. Cai. Funding was provided by the U.S. Air Force Office of Scientific Research.

REFERENCES

1. F. Deuerler, R. Knehans and R. Steinbrech, *J. Phys. (Paris)* **13,** C1 (1986).
2. P. L. Swanson, C. J. Fairbanks, B. R. Lawn, Y.-W. Mai and B. J. Hockey, *J. Am. Ceram. Soc.* **70,** 279 (1987).
3. P. L. Swanson, in *Fractography of Glasses and Ceramics*, Vol. 22, p. 135. American Ceramic Society, Columbus, Ohio (1988).
4. B. R. Lawn, *Fracture of Brittle Solids*. Cambridge University Press, Cambridge (1993).
5. S. J. Bennison and B. R. Lawn, *Acta metall.* **37,** 2659 (1989).
6. S. Lathabai, J. Rödel and B. R. Lawn, *J. Am. Ceram. Soc.* **74,** 1340 (1991).
7. J. Rödel, *J. Europ. Ceram. Soc.* **9,** 323 (1992).
8. L. M. Braun, S. J. Bennison and B. R. Lawn, *Ceram. Engng Sci. Proc.* **13,** 156 (1992).
9. L. M. Braun, S. J. Bennison and B. R. Lawn, *J. Am. Ceram. Soc.* **75,** 3049 (1992).
10. G. H. Beall, in *Advances in Nucleation and Crystallization in Glasses* (edited by L. L. Hench and S. W. Freiman), p. 251. The American Ceramic Society, Columbus, Ohio (1972).
11. C. K. Chyung, G. H. Beall and D. G. Grossman, in *Electron Microscopy and Structure of Materials* (edited by G. Thomas, R. M. Fulrath and R. M. Fisher), p. 1167. University of California Press, Berkeley, Calif. (1972).
12. K. Chyung, G. H. Beall and D. G. Grossman, in *Proceedings of 10th International Glass Congress* (edited by M. Kunugi, M. Tashiro and N. Saga), No. 14, p. 33. The Ceramic Society of Japan, Kyoto, Tokyo (1974).
13. T. Uno, T. Kasuga and K. Nakajima, *J. Am. Ceram. Soc.* **74,** 3139 (1991).
14. D. G. Grossman, in *Proceedings of the International Symposium on Computer Restorations* (edited by W. H. Mörmann), p. 103. Quintessence, Chicago (1991).
15. L. Ewart and S. Suresh, *J. Mater. Sci.* **22,** 1173 (1987).

16. S. Suresh, *Fatigue of Materials*. Cambridge University Press, Cambridge (1991).
17. F. Guiberteau, N. P. Padture, H. Cai and B. R. Lawn, *Phil. Mag. A* **68,** 1003 (1993).
18. H. Cai, M. A. Stevens Kalceff and B. R. Lawn, *J. Mater. Res.* **9,** 762 (1994).
19. F. Guiberteau, N. P. Padture and B. R. Lawn, *J. Am. Ceram. Soc.* **77,** 1825 (1994).
20. H. Cai, M. A. S. Kalceff, B. M. Hooks, B. R. Lawn and K. Chyung, in preparation.
21. H. H. K. Xu, L. Wei, N. P. Padture, B. R. Lawn and R. L. Yeckley, *J. Mater. Sci.* In press.
22. N. P. Padture and B. R. Lawn, *J. Am. Ceram. Soc.* **77,** 2518 (1994).
23. B. R. Lawn, N. P. Padture, H. Cai and F. Guiberteau, *Science* **263,** 1114 (1994).
24. N. P. Padture and B. R. Lawn, *J. Am. Ceram. Soc.* In press.
25. H. K. Xu and S. Jahanmir, *J. Mater. Sci.* In press.
26. N. P. Padture, *J. Am. Ceram. Soc.* **77,** 519 (1994).
27. M. V. Swain and B. R. Lawn, *Physica status solidi* **35,** 909 (1969).
28. D. Tabor, *Hardness of Metals*. Clarendon Press, Oxford (1951).
29. B. R. Lawn, N. P. Padture, F. Guiberteau and H. Cai, *Acta metall. mater.* **42,** 1683 (1994).
30. H. Horii and S. Nemat-Nasser, *J. Geophys. Res.* **90,** 3105 (1985).
31. H. Horii and S. Nemat-Nasser, *Phil. Trans. R. Soc. Lond.* **319,** 337 (1986).
32. M. F. Ashby and S. D. Hallam, *Acta metall.* **34,** 497 (1986).
33. J. M. Kemeny and N. G. W. Cook, in *Toughening Mechanisms in Quasi-Brittle Materials* (edited by S. P. Shah), pp. 287–311. Kluwer, Dordrecht (1991).
34. F. C. Frank and B. R. Lawn, *Proc. R. Soc. Lond.* **A299,** 291 (1967).
35. J. C. Jaeger and N. G. W. Cook, *Fundamentals of Rock Mechanics*. Chapman & Hall, London (1971).
36. F. P. Bowden and D. Tabor, *The Friction and Lubrication of Solids*. Clarendon Press, Oxford (1986).
37. K. L. Johnson, *Contact Mechanics*. Cambridge University Press, London (1985).
38. R. H. Dauskardt, *Acta metall. mater.* **41,** 2765 (1994).
39. X. Dong, S. Jahanmir and S. M. Hsu, *J. Am. Ceram. Soc.* **74,** 1036 (1991).
40. B. J. Hockey and S. M. Wiederhorn, *J. Am. Ceram. Soc.* **75,** 1822 (1992).
41. S. v. D. Zwagg, J. T. Hagan and J. E. Field, *J. Mater. Sci.* **15,** 2965 (1980).
42. N. P. Padture, C. J. Evans, H. H. K. Xu and B. R. Lawn, *J. Am. Ceram. Soc.* In press.